

A nanofilter for fluidic devices by pillar-assisted self-assembly microparticles

Tamer AbdelFatah, Mahsa Jalali, and Sara Mahshid^{a)}

Department of Bioengineering, McGill University, Montreal, Quebec H3A 0E9, Canada

(Received 16 July 2018; accepted 2 November 2018; published online 19 November 2018)

We present a nanofilter based on pillar-assisted self-assembly microparticles for efficient capture of bacteria. Under an optimized condition, we simply fill the arrays of microscale pillars with submicron scale polystyrene particles to create a filter with nanoscale pore diameter in the range of 308 nm. The design parameters such as the pillar diameter and the inter-pillar spacing in the range of 5 μm -40 μm are optimized using a multi-physics finite element analysis and computational study based on bi-directionally coupled laminar flow and particle tracking solvers. The underlying dynamics of microparticles accumulation in the pillar array region are thoroughly investigated by studying the pillar wall shear stress and the filter pore diameter. The impact of design parameters on the device characteristics such as microparticles entrapment efficiency, pressure drop, and inter-pillar flow velocity is studied. We confirm a bell-curve trend in the capture efficiency versus inter-pillar spacing. Accordingly, the 10 μm inter-pillar spacing offers the highest capture capability (58.8%), with a decreasing entrapping trend for devices with larger inter-pillar spacing. This is the case that the 5 μm inter-pillar spacing demonstrates the highest pillar wall shear stress limiting its entrapping efficiency. As a proof of concept, fluorescently labeled *Escherichia coli* bacteria (*E. coli*) were captured using the proposed device. This device provides a simple design, robust operation, and ease of use. All of which are essential attributes for point of care devices. *Published by AIP Publishing.* <https://doi.org/10.1063/1.5048623>

I. INTRODUCTION

Direct and efficient capture of a low number of bacteria from body fluids (such as nasal swap) can lead to the sensitive detection of bacterial infections. Standard clinical approaches include culture/c colony counting techniques, molecular diagnostics based on polymerase chain reaction (PCR),¹ and enzyme linked immunosorbent assay (ELISA).² Yet, they suffer from being laborious, time-consuming and requiring complex and expensive equipment, long periods to produce results (3-4 days), and 5-7 days for validation.³

Compared to classical approaches, micro/nanofluidics offer the ability of precise manipulation of small amounts of fluid (10^{-18} to 10^{-6} l), short analysis time, low sample/reagents consumption, and economically inexpensive test methods.⁴⁻⁸ More prominently, a single microfluidic device can perform a complete set of functions ranging from sample concentration to separation and detection.⁹ Current challenges faced by microfluidic technologies are lack of enough sensitivity and throughput for detection of low concentration of analytes to use in point-of-care settings. Recently, microfluidic based sample delivery systems are integrated with electrokinetic, centrifugal, and magnetic forces or functionalized with biological probes (such as an antibody) to address these challenges.

Electro-kinetic microfluidics are strongly dependent on the force experienced by particles carrying net charge in the presence of uniform or non-uniform electric fields.¹⁰⁻¹² This approach

^{a)}Author to whom correspondence should be addressed: sara.mahshid@mcgill.ca

has been widely investigated for sample concentration in fluidic devices.¹³ Islam *et al.*¹⁴ applied electrophoresis for capture and electric lysis of *E. coli* using a nanoporous membrane. The device operation was a two-step scheme with a capturing step at lower electric field and an electric lysis step at high electric field. Qiao *et al.*¹⁵ developed a two-stage electrophoretic device for DNA capture and enrichment with an enrichment factor of 2790. Madiyar *et al.*¹⁶ proposed a dielectrophoresis (DEP) device based on nanoelectrode arrays of vertically aligned carbon nanofibers for capture and detection of microbes such as bacteria and viruses with a limit of detection of 1–10 cfu ml⁻¹ for viruses. In another attempt, del Moral Zamora *et al.*^{17,18} proposed an automated DEP device for continuous flow concentration and detection of *E. coli* using the impedance measurement technique versus accumulation of bacteria.

Centrifugal microfluidics¹⁹ depend on the centrifugal force generated by a rotating device. It does not require a complex pumping system but rather a simple motor and no external instrumentation. Wiederoder *et al.*²⁰ proposed a hyper polymer-paper centrifugal device for sample enrichment, mixing, and integration of sequential assay steps using *E. coli* bacteria. Another interesting approach by Chen *et al.*²¹ is based on centrifugal microflows driven by ionic wind generated near the tip of a corona needle held above a small reservoir. They used their device for pre-concentration and capture of *Neisseria* and *Salmonella* bacteria with a limit of detection of 2300 cfu ml⁻¹.

Immunocapture microfluidics²² depends on a specific interaction between the target surface marker and an antibody, which is chemically linked to the surface of the substrate providing high specificity toward the target of interest. Tsougeni *et al.*²³ proposed a device based on immunoaffinity for capture and thermal lysis of *Salmonella* in the range of 10²–10⁸ cells ml⁻¹. The device featured a plasma treated surface for increasing the surface area and thus the antibody binding capacity.²³ Wang *et al.*²⁴ proposed a sandwich immunoassay based on monoclonal goat anti-*S. typhimurium* antibody for capture of *Salmonella*. Next, the captured bacteria were labeled with quantum dots (QD) as a fluorescent marker using QDs–IgG–primary antibody and was detected *in situ* using a self-assembly light-emitting diode-induced fluorescence detection (LIF) microsystem. This improved the detection sensitivity and the detection limit to 37 cfu ml⁻¹.

Recently, integrated fluidic devices based on nanostructured materials and immunoaffinity detection assays have shown potential applications in high throughput detection of bacteria.²⁵ We have developed an integrated microfluidic device that combines a nanostructured detection platform with an immunocapture assay for specific capture of methicillin-resistant-*Staphylococcus aureus* (MRSA) with a limit of detection of 50 cfu ml⁻¹.²⁵ The integrated device features a nanoscale filter based on pillar-assisted self-assembly microparticles (PSMP), to avoid escape of bacteria from the analysis chamber.

In particular, filter based microfluidics^{26,27} depend on physical constrictions (porous membranes or tightly packed structures or nanopatterned features) to manipulate floating target molecules inside the fluidic device. For example, microscale pillar arrays have been previously used for untangling single DNA molecules (~k base pairs) in micro/nanofluidic devices.^{8,28,29} Periodic pillar arrays were used for particle size-based separation through the use of deterministic lateral displacement arrays.^{30,31} This method relies on the fact that the flow path of microparticles between the pillar array region differs depending on the particle size. Huang *et al.*³² introduced a mixture of 0.8, 0.9, and 1 μm to the device and achieved sorting of different microparticles in 40 s with a resolution of ~10 nm.

In this paper, we aim to discuss the design optimization parameters such as the pillar diameter and the inter-pillar spacing for design and fabrication of a PSMP nanofilter. The underlying dynamics of microparticles self-assembly in the region of pillar arrays will be discussed thoroughly by studying the pillar wall shear stress and the filter pore diameter by using a multi-physics finite element analysis study. The proposed PSMP nanofilter is simply assembled by filling the arrays of microscale pillars with microscale polystyrene particles. The PSMP nanofilter features nanoscale pores with 308 nm pore diameter, small enough for the capture of bacteria (such as *E. coli* ~1 μm). Numerical study based on bi-directionally coupled laminar flow and particle-tracking solvers is carried out for studying design optimization parameters and for device performance evaluation. The results are validated with the experimental study of *E. coli* capture.

II. EXPERIMENTAL SECTION

A. Computational study using COMSOL simulation

The goal of this study is to define the optimum design parameters for the pillar-assisted self-assembly microparticles (PSMP) based nanofilter for bacterial capture. We used COMSOL Multiphysics 5.3a software (COMSOL Inc., Burlington, MA) to assess the device performance through finite element analysis simulations. The COMSOL geometry consists of a 2D sketch of the microfluidic chamber ($1.5\text{ mm} \times 3\text{ mm} \times 50\mu\text{m}$) and arrays of pillars with different designs in terms of diameter and inter-pillar spacing. We did a multi-physics COMSOL simulation by solving laminar flow and particle trajectory tracing modules simultaneously.

In this simulation, a bidirectionally coupled particle tracing for fluid flow study was applied. The coupling between microparticles conservation of momentum and the Navier-Stokes equation can be done in COMSOL software by introducing a volume force term [defined by $F_V(r)$] to the latter, where the volume force is equal in magnitude and opposite in direction to the total drag force (F_D) that the fluid exerts on microparticles. Thus, the Navier-Stokes equation for incompressible single-phase fluid in the laminar flow regime can be reduced to

$$\rho \frac{\partial \mathbf{u}}{\partial t} + \rho(\mathbf{u} \cdot \nabla) \mathbf{u} = \nabla \cdot [-p\mathbf{I} + \mu (\nabla \mathbf{u} + (\nabla \mathbf{u})^T)] + \mathbf{F}, \quad (1)$$

$$\rho \nabla \cdot \mathbf{u} = 0, \quad (2)$$

where \mathbf{u} (SI unit: m/s) is the fluid velocity, p (SI unit: Pa) is the pressure, ρ (SI unit: kg/m³) is the density, μ (SI unit: Pa s) is the dynamic viscosity, and \mathbf{F} (SI unit: N) is the total volume force.

To calculate the contribution of particle motion to the total volume force acting on the fluid (F_v), we calculate the drag force that the fluid exerts on PSB

$$\frac{d}{dt}(m_p v) = F_D + F_g + F_{ext}, \quad (3)$$

$$F_D = \left(\frac{1}{\tau_p} \right) m_p (u - v), \quad (4)$$

$$\tau_p = \frac{\rho_p d_p^2}{18\mu}, \quad (5)$$

where m_p is the particle mass (SI unit: kg), v is the velocity of the particle (SI unit: m/s), F_D is the drag force (SI unit: N), F_g is the gravitational force (SI unit: N), F_{ext} is any other external force (SI unit: N), τ_p is the particle velocity response time (SI unit: s), u is the fluid velocity (SI unit: m/s), μ is the fluid viscosity (SI unit: Pa s), ρ_p is the particle density (SI unit: kg/m³), and d_p is the particle diameter (SI unit: m).

Given an array of idealized point masses such that the position vector of the i th particle is denoted q_i (SI unit: m), the volume force at position r is

$$F_V(r) = - \sum_{i=1}^N F_{D,i} \delta(r - q_i), \quad (6)$$

where δ is the Dirac delta function, $F_{D,i}$ is the drag force exerted on the i th particle, and N is the total number of particles. The favorable PSP entrapping in the pillar array region conditions is

when the total forces opposing the drag force (volume force and PSPs/pillar interaction forces) are equal to or higher than the drag force. This is the condition when the streamline carrying the PSP moves in the near proximity of the pillar (spacing between streamline and pillar \approx PSP radius) or ends abruptly at the pillar.

The inlet boundary condition was set to constant velocity ($10\ \mu\text{L}/\text{min}$) and one-time initial release of 1000 particles, while the outlet boundary condition was set to constant pressure (atmospheric pressure) with particle freeze conditions. All other interfaces were considered as walls using the no slip and freeze boundary conditions. Water was considered as the working fluid. We used a free triangular mesh with a total of 27 145 elements.

B. Design and fabrication of the microfluidic device

The device was designed using AutoCAD® (Autodesk Inc., CA, USA) and printed on a flexible photomask. Near UV photolithography was used to fabricate the microfluidic features in a SU-8 layer (SU-8 2025, MicroChem Corp., MA, USA) on top of a 4 in. glass substrate, which was then diced to make 9 devices. Next, inlet and outlet ports were punched in polydimethylsiloxane (PDMS SYLGARD 184 silicone elastomer, Dow Consumer Solutions, QC, Canada) and bonded to the device surface using established protocols.^{25,33} Briefly, PDMS was plasma treated and put in contact with the SU-8 device under pressure and left for curing overnight at $100\ ^\circ\text{C}$ to create an irreversible bond between SU-8 and PDMS.

C. Fabrication of the pillar-assisted self-assembly microparticles filter

Polystyrene particles (PSP, Fluorescent Nile Red Particles FP-2056-2, Spherotech, Lake Forest, IL) were used as the microparticles to fill the micropillar arrays and to create the nanoscale filter. Initially, ethanol was added to the PSP aliquots to stabilize the PSP at the water/air interface and minimize aggregation during the pillar assisted self-assembly process.³⁴ Next, fluorescent-labeled microparticles with $2\ \mu\text{m}$ in diameter were used to experimentally verify the self-assembly process. A $1.22\ \mu\text{l}$ suspension of $2.274 \times 10^8\ \text{PSP}\ \text{ml}^{-1}$ in ethanol was pipetted in the inlet port and flown toward the micropillar arrays with an average flow rate of $3.1\ \mu\text{l}\ \text{min}^{-1}$. Subsequently, phosphate buffer saline ($1 \times$ PBS) was pipetted with an average flow rate of $3.1\ \mu\text{l}\ \text{min}^{-1}$ to wash out the excess particles from the bacteria-trapping chamber. Lastly, the device was placed in a vacuum chamber for 90 min as a drying step to eliminate the presence of ethanol due to its anti-bacterial properties. After the drying step, the device was ready for the bacterial capture process. A motorized inverted confocal microscope (IX83 Olympus) was used to observe the movement of the PSP particles and the self-assembly event. At the end, Mcherry and green fluorescent protein (GFP) labeled *Escherichia coli* K12 bacteria (*E. coli* in LB media) were used to evaluate the device trapping performance and bacteria escape percentage.

III. RESULTS AND DISCUSSION

Figure 1(a) shows a schematic representation of the microfluidic device featuring a region of micro-pillar arrays between a trapping chamber ($1.5\ \text{mm} \times 3\ \text{mm} \times 50\ \mu\text{m}$) and outlet micro-channels ($400\ \mu\text{m} \times 50\ \mu\text{m}$). The fluids are introduced through an inlet port to the micro-channels and into the trapping chamber. At the interface of the trapping chamber and the outlet channel, the micro-pillar arrays are filled with PSP to create a nanoscale fluidic region, which traps the bacteria inside the trapping chamber, while allowing the fluid to pass through the pillar arrays and flow through micro-channels into the outlet port.

Figure 1(b) shows the final prototype ($20\ \text{mm} \times 20\ \text{mm}$) consisting of individual fluidic compartments with separate inlets/outlets, featuring small footprint modules for handling multiple sample solution.

We use a two-step process to fabricate the PSMP nanofilter based device. First, the device geometry is defined on a SU-8 coated glass substrate using a single mask lithography step and then bonded to a PDMS layer. Figure 1(c) shows the optical image of the micro-pillar arrays patterned

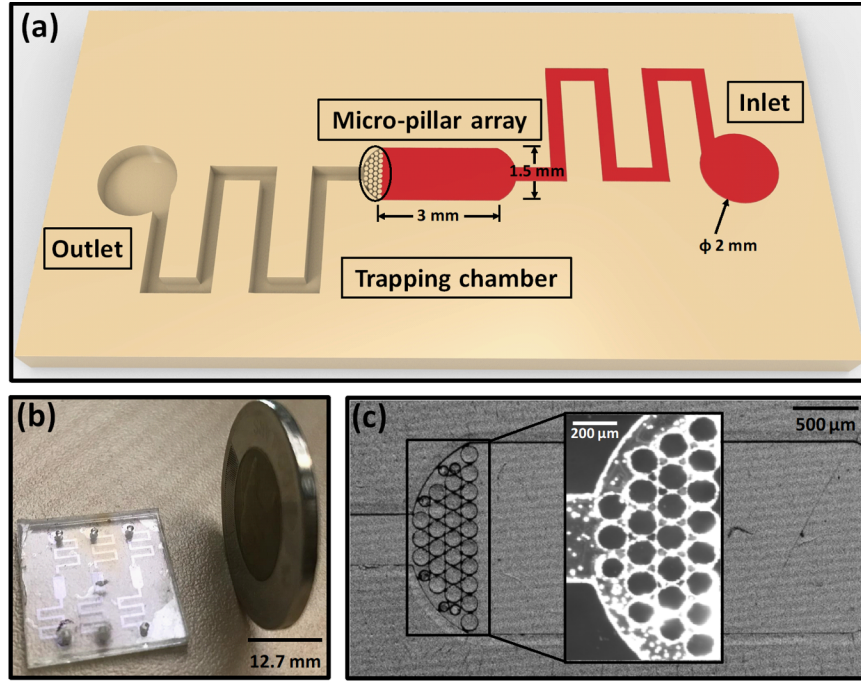


FIG. 1. Bacteria trapping device. (a) Schematic representation of the bacteria trapping device, consisting of microfluidic channels ($400\text{ }\mu\text{m} \times 50\text{ }\mu\text{m}$) connecting inlet/outlet ports to a trapping chamber ($1.5\text{ mm} \times 3\text{ mm} \times 50\text{ }\mu\text{m}$). Micro-pillar arrays are used to trap the target bacteria (*E. coli*). (b) Trapping module ($20\text{ mm} \times 20\text{ mm}$) containing 3 microfluidic devices. (c) 4x microscopy image of a $10\text{ }\mu\text{m}$ inter-pillar spacing trapping device with an inset fluorescent image of PSP filled pillar area.

on SU-8. Lastly, the micro-pillar arrays are filled with injected PSP, followed by a washing step to create a region of PSMP [Fig. 1(c), inset]. The entrapment of PSPs in the pillar array region is resulting from the use of high concentration of PSPs to get entrapped in a structure with a gap bigger than their diameter. This is called the keystone effect^{35–37} and was utilized by Ceriotti *et al.*³⁸ to entrap a high concentration of $3\text{ }\mu\text{m}$ particles in a $16\text{ }\mu\text{m}$ gap.

The entrapped PSP turns the pillar region to a filter with nanoscale pore diameter, which can be simply calculated using hexagonal close packing configuration with a packing fraction of 0.74.³⁹ Figure 2(a) schematically visualizes red spheres in hexagonal close packing configuration. In this figure, the pore diameter (represented by a blue spherical particle) is determined using the following equation:

$$D_p = 0.154D_s, \quad (7)$$

where D_p is the diameter of the pores and D_s is the diameter of the spheres. For $2\text{ }\mu\text{m}$ PSP, the pore diameter is $0.308\text{ }\mu\text{m}$.

Figures 2(b) and 2(c) show the experimental results of entrapped PSPs within the micropillar arrays under $20\times$ and $40\times$ magnification, respectively. Due to the confined space in the designed microfluidic device, there is a limited water/air interface to form a PSP self-assembled layer which leads to multi-layered aggregation of PSPs. A mixture of PSP and ethanol was used to enhance the stabilization of PSPs at the water/air interface to some extent and minimize the aggregation of PSPs.³⁴ The pore diameter was estimated around $0.319\text{ }\mu\text{m}$ using Image J software, which is in a good agreement with the theoretical value. This confirms our hypothesis for creating a filter with nanoscale pores for the capture of microscale biological targets such as bacteria.

In Sec. III A, we use a multi-physics COMSOL simulation based on bi-directionally coupled laminar flow and particle tracing solvers to discuss the optimization parameters such as the pillar

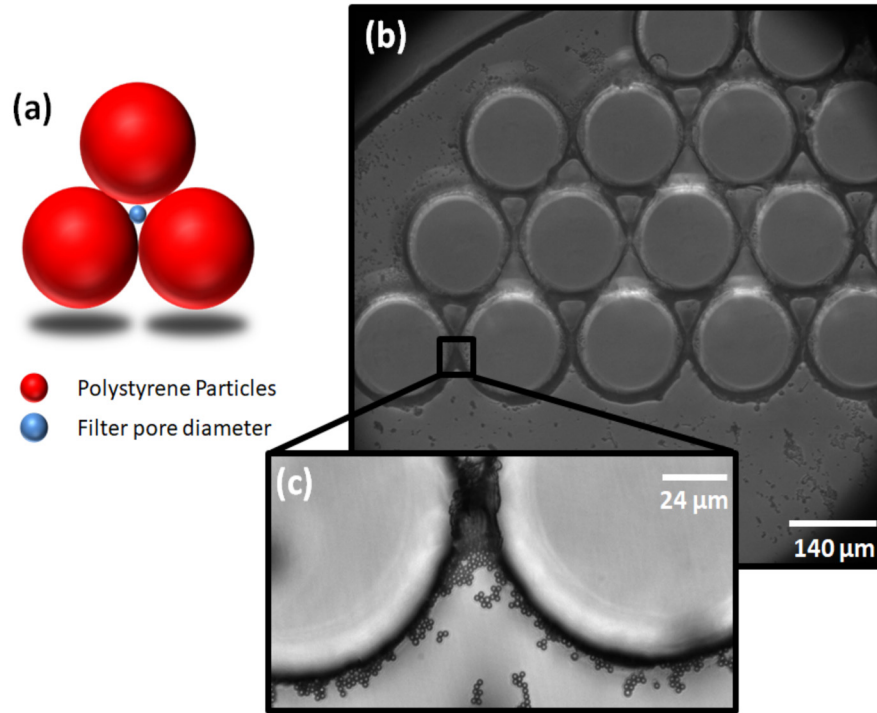


FIG. 2. PSP accumulation dynamics and filter pore diameter estimation. (a) A representation of accumulated PSP (red spheres) in hexagonal close packing structure with the blue sphere representative of the pore diameter. (b)–(c) Microscopic image of entrapped PSPs in pillar arrays area with 20 \times and 40 \times zoom, respectively.

diameter and the inter-pillar spacing and to evaluate the underlying dynamics of PSP self-assembly in the pillar arrays.

A. Computational study of the fluidic characteristics

We applied a 2D COMSOL multi-physics simulation to assess PSP entrapping performance for different device geometries. Figures 3(a)–3(e) represent the proposed geometries with a different inter-pillar spacing of 5, 10, 15, 20, and 40 μm , respectively. We chose the current dimensions for favorable fabrication conditions. Using smaller inter-pillar spacing would inherently introduce more challenging fabrication requirement, due to higher aspect ratio structures. We evaluate the impact of the design parameters on the device characteristics such as (1) PSP entrapment efficiency, (2) pressure drop, and (3) inter-pillar flow velocity.

First, we study the effect of the inter-pillar spacing on the pressure drop for different geometries. Figure 4(a) shows the pressure drop profile within the device and the micropillar arrays. From the pressure profile in Fig. 4(a), it is clear that the region of pillar arrays represents the highest flow resistance and pressure drop. Figure 4(b) shows the pressure distribution inside the pillar arrays along a cut line in the middle of the geometry [represented by a red line in Fig. 4(d)]. The plot shows nearly constant pressure values before and after the pillar arrays, and an abrupt steep pressure drop ($\sim 90\%$ of the overall pressure drop) within the boundaries. Figure 4(c) represents the overall pressure drop for different inter-pillar spacing, ranging from 9870 Pa for 5 μm inter-pillar spacing to 85.9 Pa for 40 μm inter-pillar spacing.

Second, we study the effect of the inter-pillar spacing on the inter-pillar velocity. Figure 4(d) shows the streamlines in the pillar arrays extracted from COMSOL simulation. The fluorescent image in Fig. 4(e) experimentally shows the flowing pattern of PSP through the analysis well and the pillar region, which is in agreement with the numerical simulation result presented in Fig. 4(d). The higher streamline density inside the pillar region [Fig. 4(d)] indicates higher flow velocity,

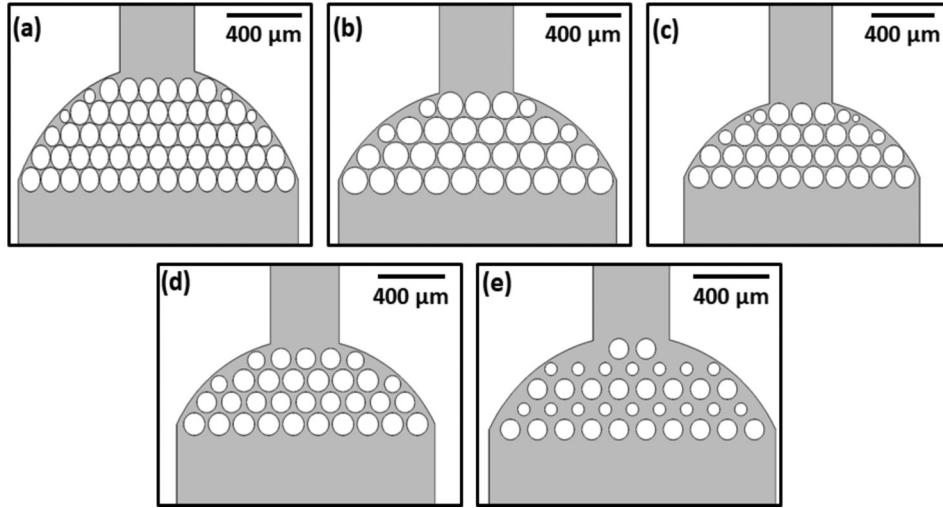


FIG. 3. Different proposed device geometries. (a)–(e) 2D models for 5, 10, 15, 20, and 40 μm inter-pillar array spacing, respectively. Different inter-pillar arrays spacing geometries are investigated using numerical simulation software package COMSOL Multiphysics to establish the optimum design for the micro-pillar arrays.

which is due to the geometrical constraints. The laminar flow regime can be observed by the parallel streamlines in both numerical and experimental results. Figure 4(f) represents a 10- to 80-fold increase in the velocity—compared with inlet velocity—for different geometries with inter-pillar spacing from 40 μm to 5 μm , respectively.

B. Study the device PSP entrapment performance

The optimum design parameters such as pillar's dimension and inter-pillar spacing are determined by using COMSOL simulation results of the PSP entrapping regime. We define “particle entrapment” parameter to determine the efficiency of entrapping PSP in the pillar arrays according to Eq. (8). A counter was used to count the PSP escaping the pillar area:

$$\text{Particle entrapment} = \frac{\text{Total released particles} - \text{Escaped particles}}{\text{Total released particles}} \times 100. \quad (8)$$

Figure 5(a) shows the total number of PSPs captured by each row within the pillar arrays for different device geometries. We observe a similar trend for all the proposed geometries, in which the upstream rows can capture more PSP compared to the further downstream rows.

The particle entrapment efficiency results [calculated from Eq. (8)] in Fig. 5(b) show a bell-shaped trend between the number of entrapped PSPs versus inter-pillar spacing. As shown in Fig. 5(b) under the simulation conditions, it is evident that the 10 μm inter-pillar spacing has the highest particles retention capabilities (58.8%) followed by the 15 μm geometry (53.9%). Contrary to the initial assumption, the 5 μm model with the smallest inter-pillar spacing does not represent the highest particle entrapment efficiency (only 50% particle entrapment efficiency).

We also numerically studied the transient time (defined as the time needed to reach the steady state condition for filling the pillars) versus inter-pillar spacing as shown in Fig. 6. All the proposed geometry represents short transient time and reaches the steady state in a few seconds. Figure 6 (inset) compares the numerical results of the steady state (filled) PSMP nanofilter for 10 μm , 5 μm , and 20 μm inter-pillar spacing geometries.

We studied the reason behind the deteriorating performance of the pillars with 5 μm inter-pillar spacing by looking at the forces applied to PSP between pillars as described below. Figure 7(a) shows a PSP with diameter r , flowing along a streamline. The figure shows a constriction area between two pillars with a pressure driven fluid, moving with velocity $U(Z)$ and exerting viscous

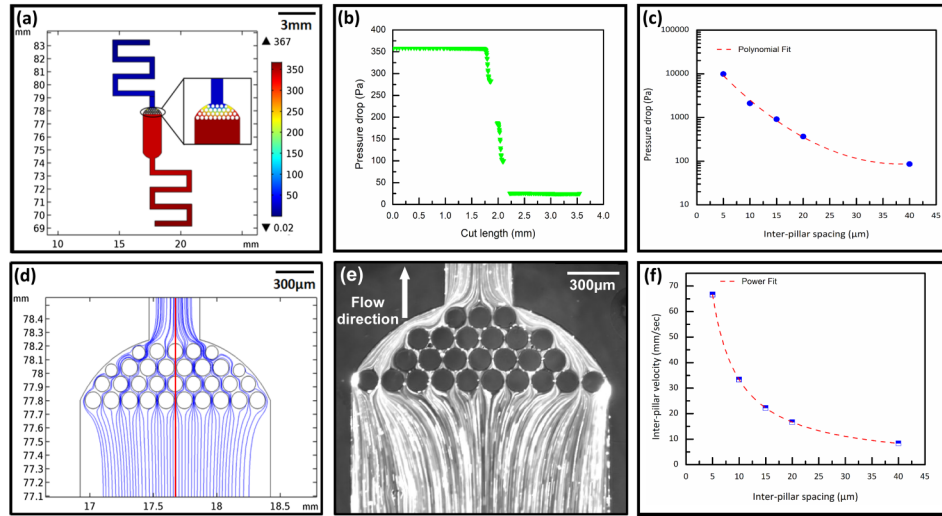


FIG. 4. Device pressure and velocity characteristics. (a) Total pressure drops versus different inter-pillar spacing geometries. Smaller inter-pillar spacing is associated with higher pressure drop due to higher flow resistance. (b) Pressure drop across the pillar arrays as shown by Pressure distribution versus cut line length (shown in 4d as a red line) plot. (d) Fluid streamlines inside the pillar arrays. Fluid velocity is generally at much higher speeds in the pillar arrays region due to the constricted area. This is evident by higher streamline density in the constricted area. (e) 4 \times fluorescent microscopy image of PSP filling the pillar region. The experimental results show a good agreement with the flow pattern estimated by the numerical simulation. (f) Inter-pillar flow velocity for different inter-pillar spacing geometries. Higher fluid velocities are associated with smaller inter-pillar spacing.

friction force F_{vf} on the pillar walls. The friction force is acting on the pillar walls and the entrapped PSP and can be calculated using the following set of equations:

$$F_{vf} = \tau_{wall} \times A_{pillar}, \quad (9)$$

$$\tau_{wall} = 2\eta G_m, \quad (9a)$$

$$G_m = \frac{4}{H} U_m, \quad (9b)$$

$$U_m = 1.5 U_{ave}, \quad (9c)$$

where F_{vf} is the viscous friction force, τ_{wall} is the shear stress induced by the fluid flow at the pillar walls, A_{pillar} is the circumference area of the pillars, η is the fluid viscosity, G_m is the maximum shear rate at the pillar wall,⁴⁰ U_m is the maximum velocity of cross-section flow, H is the inter-pillar thickness, and U_{ave} is the average velocity of cross-section flow.

We establish the viscous friction force (F_{vf}) values for different device inter-pillar spacing and present the results in Fig. 7(b). We first start by calculating the average flow velocity between the pillars (U_{ave}) by dividing the flow rate by the cross-sectional area between the pillars (inter-pillar spacing \times pillar height). Next, the maximum flow velocity (U_m) between the pillars is evaluated using Eq. (9c). Using the obtained U_m , we estimate the maximum shear rate at the pillar wall (G_m). The pillar wall shear stress (τ_{wall}) is evaluated using Eq. (9a) by substituting the calculated value of G_m and the fluid dynamic viscosity. Lastly, the shearing viscose friction force is calculated by multiplying τ_{wall} and the pillar's surface area. Since each device contained different pillar diameters, the total pillar surface area is the summation of their surface areas as shown by $\sum \pi n_D D L$, where n_D is the number of pillars having a certain diameter (D), D is the pillar diameter extracted from COMSOL geometry in Fig. 3, and L is the pillar height (50 μ m). Figures 7(c) and 7(d) represent the total pillar area and the wall shearing stress (τ_{wall}) versus inter-pillar spacing, respectively.

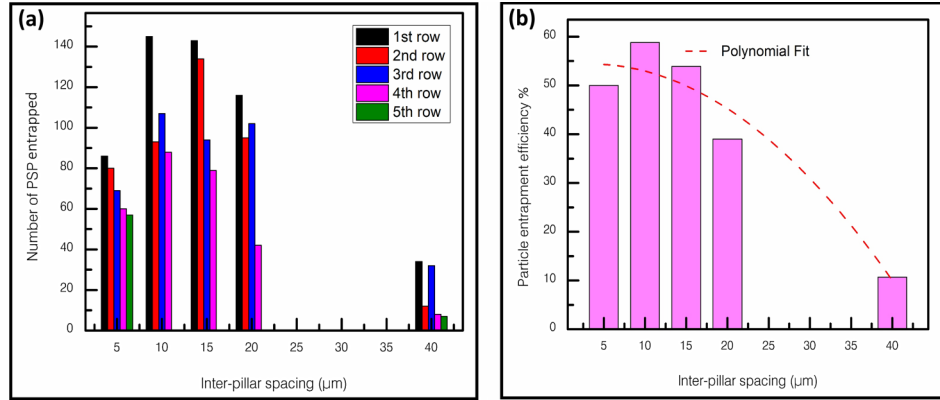


FIG. 5. The number and efficiency of entrapped PSPs versus different devices. (a) Number of PSPs entrapped per row for different device geometries. There is a consistent pattern for higher PSP entrapping for upstream rows than downstream rows for all proposed designs. (b) Particle entrapment efficiency for different device geometries. 10 μm and 15 μm inter-pillar spacing devices exhibit the highest particle entrapping efficiency making them the optimum designs.

According to the figures, the 5 μm inter-pillar spacing design exhibits both the highest shear stress values and the highest total pillar areas ($877\,033.4\,\mu\text{m}^2$). The combination of which limits the PSP entrapment efficiency by introducing 5 times higher shear viscous friction force than the next design (10 μm inter-pillar spacing) and 117 times higher shear viscous friction force than the design with the least shear forces (40 μm inter-pillar spacing), as shown by Fig. 7(b). There is a general trend of reduction in wall shear forces with increasing inter-pillar spacing. This is due to the reduction in the maximum flow velocity by increasing the constriction area. Also, a reduction trend of the total pillar area for wider spacing designs is observed. The combination of which leads to a reduction in the friction force with wider pillar spacing.

We also studied the relationship between the pillar size and the average number of entrapped PSPs (see Fig. 8). From Fig. 7(c), the 10 μm and 15 μm designs featured $6.56 \times 10^5\,\mu\text{m}^2$ and $6.4 \times 10^5\,\mu\text{m}^2$ total pillar surface area, respectively (varying from $8.77 \times 10^5\,\mu\text{m}^2$ to $4.81 \times 10^5\,\mu\text{m}^2$). Figure 8(a) demonstrates the calculated average PSPs entrapped per pillar for different pillar

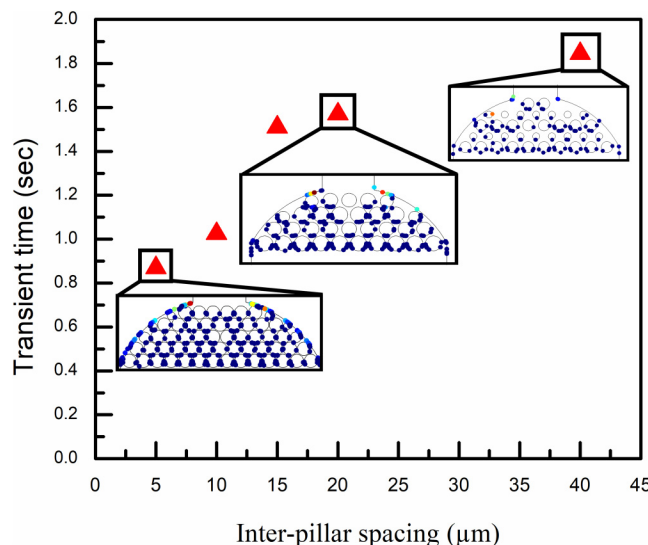


FIG. 6. Transient time of filling the pillars for different geometries. Plot of time needed to reach the steady state condition for filling the pillars for different inter-pillar spacing geometries. The designs exhibit a rapid operation reaching steady state in approximately 2 s. (Inset) Comparison of numerical results of steady state for different PSMP nanofilter geometries.

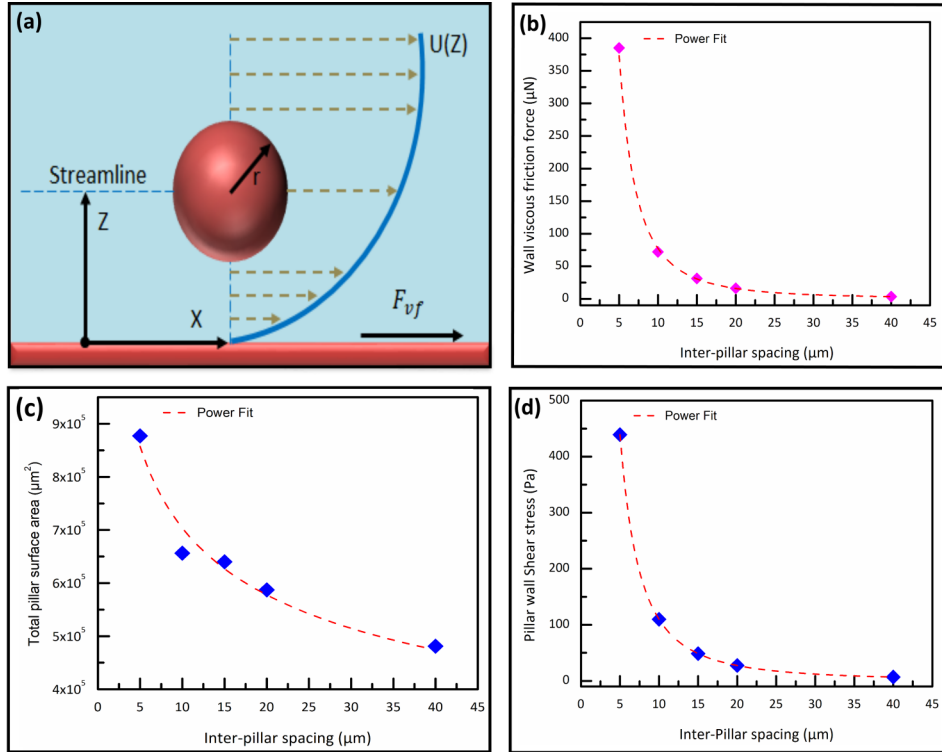


FIG. 7. Effect of inter-pillar spacing on PSP filling and shearing forces. (a) A representation of a PSP with radius r flowing along a streamline in a pressure driven flow and at a distance z from the side wall with viscous friction force F_{vf} applied by the moving fluid on the stationary wall. (b) Wall viscous friction forces for different device designs. It is noted that the $5\mu\text{m}$ geometry exhibits the highest wall viscous friction force resulting in less entrapping of PSP; this is due to high shearing stresses and higher surface area compared to other designs. (c) Total pillar surface area and (d) Pillar wall shear stress for different device designs.

diameters, while Fig. 8(b) shows the total pillar surface area for different designs versus average captured PSP per pillar indicating the average PSB captured per pillar for different device designs. In order to observe the effect of changing pillar diameter on PSP entrapment, we studied a general trend of higher PSP entrapment with larger pillar diameter except for the pillar with $137.2\mu\text{m}$

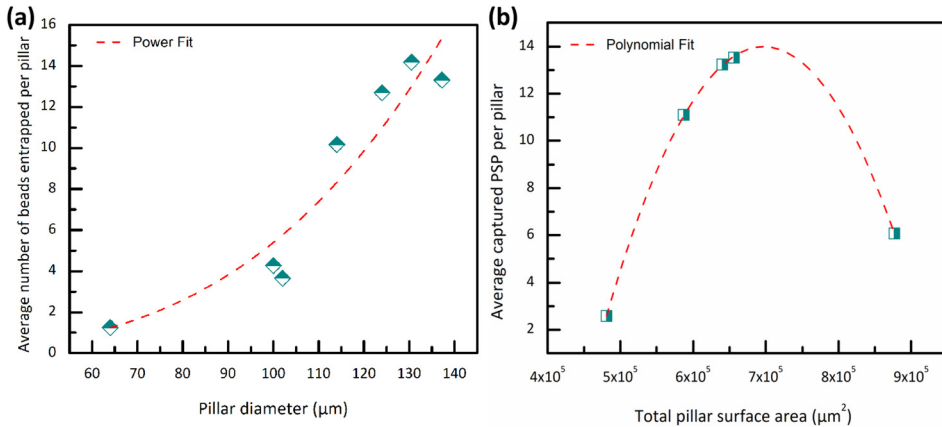


FIG. 8. Relation between the pillar size and the average captured PSP per pillar. (a) Average number of PSPs entrapped per pillar for different pillar diameters. There is a general trend of higher average PSPs entrapping per pillar for bigger diameter pillars. (b) Total pillar surface area versus average captured PSP per pillar. Larger total pillar surface area devices exhibit higher PSP entrapped per pillar, the only exception of this is the $5\mu\text{m}$ device which is affected by high pillar wall shear stresses compromising its PSP entrapping performance.

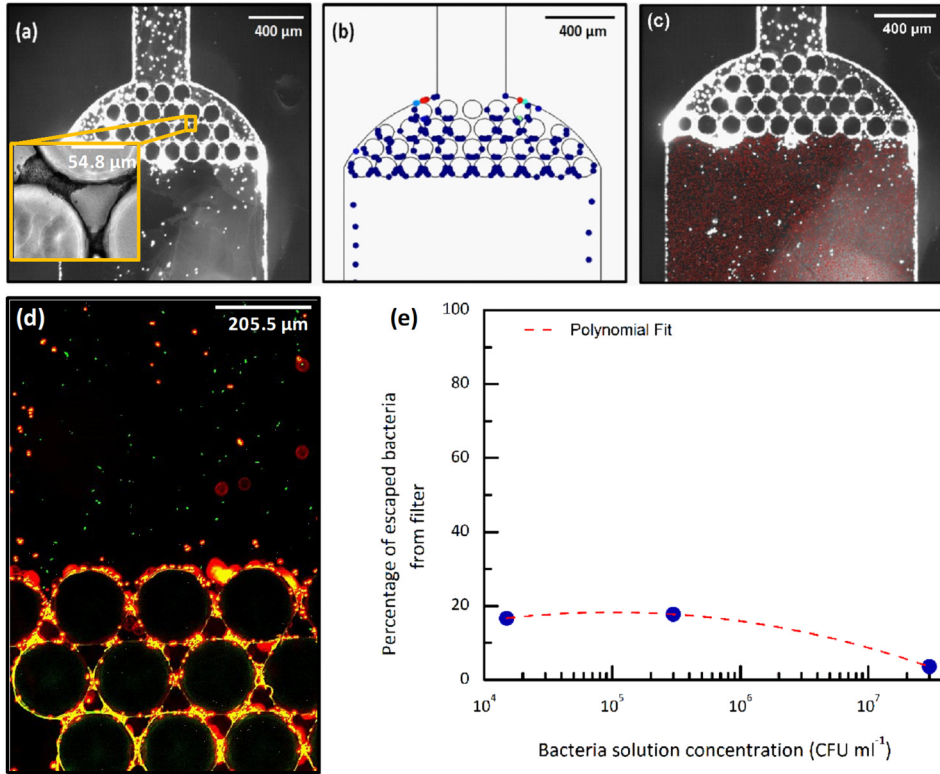


FIG. 9. PSP self-assembly and bacteria trapping. (a) 4 \times fluorescent images of entrapped PSP and 40 \times microscopic image inset showing entrapped PSP. The entrapped PSP was pipetted to the device and subsequently undergone a washing step using PBS. (b) PSP entrapping in the device as predicted by numerical simulation. The experimental results are in a good agreement with the numerical predictions shown previously. (c) 4 \times fluorescent image of trapped *E. coli*. Bacteria showing efficient bacteria capturing, note a virtual coloring scheme was applied to highlight trapped bacteria for better result representation. (d) 10 \times fluorescent image (binary image) for PSP filled pillar region trapping *E. coli* bacteria (shown in green). The image is the result of a combination of red and green channel images for the same region; note that the PSPs appear in yellow color as they have a wide emission spectrum and thus they appear in both red and green images, while GFP labelled *E. coli* bacteria appears only in green color. (e) Percentage of bacteria escaping the filter versus bacteria concentration (CFU ml⁻¹). The plot shows the low bacteria escape for different concentrations.

which is associated with the 5 μm inter-pillar spacing design (this design exhibited higher wall shear forces limiting the PSPs entrapment). We confirmed the resulting trend through plotting total pillar surface area for different designs versus average PSP entrapped per pillar [Fig. 8(b)], which shows a general trend of higher PSP entrapment with larger total pillar surface area. As previously discussed, the only exception is the 5 μm design, which is associated with high wall viscous shearing forces. In conclusion, the 10 μm and 15 μm devices are the optimum designs.

C. Proof of concept bacterial capture

The bacteria trapping performance of the device was experimentally evaluated as a proof of concept. *E. coli* samples were received from culture media and were split into aliquots with 15×10^3 CFU ml⁻¹, 3×10^5 CFU ml⁻¹, and 3×10^7 CFU ml⁻¹ concentrations that were identified by a spectrophotometer. For bacteria trapping and visualization experiments, a 5 μl of 3×10^7 CFU ml⁻¹ *E. coli* sample was pipetted to the device at an average flow rate of 4 $\mu\text{l min}^{-1}$. While for estimating bacteria escaping percentage, a 2 μl of *E. coli* sample was pipetted to the device at an average flow rate of 4 $\mu\text{l min}^{-1}$ and the downstream of the filter was imaged and analyzed using Image J software. Figure 9(a) is a 4 \times fluorescence microscopy image of a PSP filled pillar array with a 40 \times microscopic inset image showing the pattern of the entrapped PSP. The high-resolution

microscopy image of PSP entrapment shows a minimized aggregation of the PSP layer which was achieved by treatment of PSPs with ethanol prior to injection. The pillar-assisted self-assembly microparticles filter shows the predicted entrapping pattern as predicted by the numerical simulation result [Fig. 9(b)]. Figure 9(c) is a $4\times$ fluorescent microscopy image of captured *E. coli* bacteria, a virtual coloring scheme was applied for better representation of the capturing event. *E. coli* bacteria tagged with green fluorescence protein (GFP) were used to confirm the successful capture of bacteria and differentiate between bacteria and PSP in fluorescence microscopy images. Figure 9(d) is a binary image showing the interface of the PSMP nanofilter and trapping chamber. The binary image is the result of combining red and green channel fluorescence images for the same region. The GFP tagged *E. coli* bacteria were observed as green signals in the binary image; thus, we were able to identify the presence of both PSP and *E. coli* bacteria and differentiate between them. The device was able to perform efficient capture of *E. coli*. Figure 9(e) plots the escaping bacteria for different bacteria concentration. The device exhibits low bacteria escape as shown by the curve with only 3.57% bacteria escaping at a bacterial concentration of $3 \times 10^7 \text{ CFU ml}^{-1}$.

IV. CONCLUSION

We introduced a PSMP nanofilter based microfluidic device for bacteria trapping. The device features the integration of micro-pillar arrays with polystyrene particles (PSP) to build a nano/microinterface for bacteria trapping. Numerical simulations were carried out to thoroughly discuss the device optimization parameters and the dynamics controlling the PSP entrapping regime. The design parameters such as the pillar diameter and the inter-pillar spacing in the range of $5\text{ }\mu\text{m}$ - $40\text{ }\mu\text{m}$ were optimized using multiphysics COMSOL simulation coupling bi-directionally laminar flow and particle tracking solvers. Accordingly, the $10\text{ }\mu\text{m}$ inter-pillar spacing offers the highest PSP capture capability (58.8%), with a decreasing PSP entrapping trend for devices with larger inter-pillar spacing, suggesting a bell-curve trend in the capture efficiency of the pillar arrays versus inter-pillar spacing. The device was simply fabricated by a single step lithography process of a SU-8 coated glass substrate followed by introducing PSP under the optimized condition to create the PSMP nanofilter. The pillar-assisted self-assembly microparticle filter features a nano-scale pore size of $0.308\text{ }\mu\text{m}$ to avoid bacteria ($\sim 1\text{ }\mu\text{m}$) escaping the trapping chamber, which was experimentally confirmed for *E. coli* bacteria.

ACKNOWLEDGMENTS

The authors thank the Faculty of Engineering at McGill University and Natural Science and Engineering Research Council of Canada (NSERC, G247765) for financial support. M.J. is grateful for MEDA award by the Faculty of Engineering at McGill University and T.A.F. is grateful for STEM scholarship from Abdulla Al Ghurair Foundation for Education. The authors acknowledge Nanotools-Microfab and the Facility for Electron Microscopy Research at McGill University and the Department of Bioengineering Research Facilities. The authors would like to thank CMC Microsystems for CAD tools support. In addition, the authors would like to thank Ayyappasamy Sudalaiyadum Perumal for assistance in bacterial culture and Gen Tsutsumi for assistance in COMSOL simulation.

¹M. Li, Z. Xie, Z. Xie, J. Liu, L. Xie, X. Deng, S. Luo, Q. Fan, L. Huang, J. Huang, Y. Zhang, T. Zeng, and J. Feng, *Influenza Other Respir. Viruses* **10**, 141 (2016).

²B. T. Teoh, S. S. Sam, K. K. Tan, J. Johari, J. Abd-Jamil, P. S. Hooi, and S. Abubakar, *Sci. Rep.* **6**, 1 (2016).

³F. M. E. Wagenlehner, A. Pilatz, and W. Weidner, *Int. J. Antimicrob. Agents* **38**, 51 (2011).

⁴S. Abdulwahab, A. H. C. Ng, M. Dean Chamberlain, H. Ahmado, L.-A. Behan, H. Gomaa, R. F. Casper, and A. R. Wheeler, *Lab Chip* **17**, 1594 (2017).

⁵V. Gnyawali, M. Saremi, M. C. Kolios, and S. S. H. Tsai, *Biomicrofluidics* **11**, 034104 (2017).

⁶R. Ghaemi, P. Rezai, F. R. Nejad, and P. R. Selvaganapathy, *Biomicrofluidics* **11**, 034113 (2017).

⁷J. D. Besant, E. H. Sargent, and S. O. Kelley, *Lab Chip* **15**, 2799 (2015).

⁸S. Mahshid, M. J. Ahmed, D. Berard, S. Amin, R. Sladek, S. R. Leslie, and W. Reisner, *Lab Chip* **15**, 3013 (2015).

⁹C. Zhao, Z. Ge, and C. Yang, *Micromachines* **8**, 28 (2017).

¹⁰R. Hamada, H. Takayama, Y. Shonishi, L. Mao, M. Nakano, and J. Suehiro, *Sens. Actuators B Chem.* **181**, 439 (2013).

- ¹¹D. Puchberger-Enengl, S. Podszun, H. Heinz, C. Hermann, P. Vulto, and G. A. Urban, *Biomicrofluidics* **5**, 044111 (2011).
- ¹²W. Zhang and A. D. Radadia, *Anal. Chem.* **88**, 2605 (2016).
- ¹³S. Mahshid, J. Lu, A. A. Abidi, R. Sladek, W. W. Reisner, and M. J. Ahamed, *Sci. Rep.* **8**, 1 (2018).
- ¹⁴S. Islam, A. Shahid, K. Kuryllo, Y. Li, M. J. Deen, and P. R. Selvaganapathy, *Micromachines* **8**, 45 (2017).
- ¹⁵W. Qiao, C. Wang, Z. Ding, J. Song, X. X. Wei, and Y. H. Lo, *Microfluid. Nanofluidics* **20**, 1 (2016).
- ¹⁶F. R. Madiyar, L. U. Syed, P. Arumugam, and J. Li, in *ACS Symposium Series* (American Chemical Society, 2013), pp. 109–124.
- ¹⁷B. del Moral Zamora, J. M. Álvarez Azpeitia, A. M. Oliva Brañas, J. Colomer-Farrarons, M. Castellarnau, P. L. Miribel-Català, A. Homs-Corbera, A. Juárez, and J. Samitier, *Electrophoresis* **36**, 1405 (2015).
- ¹⁸B. del Moral-Zamora, J. Punter-Villagrassa, A. M. Oliva-Brañas, J. M. Álvarez-Azpeitia, J. Colomer-Farrarons, J. Samitier, A. Homs-Corbera, and P. L. Miribel-Català, *Electrophoresis* **36**, 1130 (2015).
- ¹⁹H. Yan, Y. Zhu, Y. Zhang, L. Wang, J. Chen, Y. Lu, Y. Xu, and W. Xing, *Sci. Rep.* **7**, 1 (2017).
- ²⁰M. S. Wiederoder, S. Smith, P. Madzivhandila, D. Mager, K. Moodley, D. L. DeVoe, and K. J. Land, *Biomicrofluidics* **11**, 054101 (2017).
- ²¹Y. Y. Chen, Y. C. Fang, S. Y. Lin, Y. J. Lin, S. Y. Yen, C. H. Huang, C. Y. Yang, L. K. Chau, and S. C. Wang, *Microchim. Acta* **184**, 1021 (2017).
- ²²H.-Y. Li, V. Dauriac, V. Thibert, H. Senechal, G. Peltre, X.-X. Zhang, and S. Descroix, *Lab Chip* **10**, 2597 (2010).
- ²³K. Tsougeni, G. Papadakis, M. Gianneli, A. Grammoustianou, V. Constantoudis, B. Dupuy, P. S. Petrou, S. E. Kakabakos, A. Tserepi, E. Gizeli, and E. Gogolides, *Lab Chip* **16**, 120 (2016).
- ²⁴R. Wang, Y. Ni, Y. Xu, Y. Jiang, C. Dong, and N. Chuan, *Anal. Chim. Acta* **853**, 710 (2015).
- ²⁵M. Jalali, T. AbdelFatah, S. S. Mahshid, M. Labib, A. Sudalaiyadum Perumal, and S. Mahshid, *Small* **14**, 1801893 (2018).
- ²⁶C. H. Chang and R. J. Yang, *Microfluid. Nanofluidics* **20**, 1 (2016).
- ²⁷F. Tian, J. Lyu, J. Shi, F. Tan, and M. Yang, *Sens. Actuators B Chem.* **225**, 312 (2016).
- ²⁸M. J. Ahamed, S. Mahshid, D. J. Berard, F. Michaud, R. Sladek, W. W. Reisner, and S. R. Leslie, *Macromolecules* **49**, 2853 (2016).
- ²⁹P. Zimny, D. Juncker, and W. Reisner, *Biomicrofluidics* **12**, 024107 (2018).
- ³⁰S. Feng, A. M. Skelley, A. G. Anwer, G. Liu, D. W. Inglis, S. Feng, A. M. Skelley, A. G. Anwer, and G. Liu, *Biomicrofluidics* **11**, 024121 (2017).
- ³¹J. O. Holm, S. H. Beech, J. P. Barrett, and M. P. Tegenfeldt, *Lab Chip* **11**, 1326 (2011).
- ³²L. R. Huang, E. C. Cox, R. H. Austin, and J. C. Sturm, *Science* **304**, 987 (2004).
- ³³Z. Zhang, P. Zhao, G. Xiao, B. R. Watts, and C. Xu, *Biomicrofluidics* **5**, 46503 (2011).
- ³⁴Z. Dai, Y. Li, G. Duan, L. Jia, and W. Cai, *ACS Nano* **6**, 6706 (2012).
- ³⁵A. Nagy and A. Gaspar, *J. Chromatogr. A* **1304**, 251 (2013).
- ³⁶J. O. Beech and J. P. Tegenfeldt, *Microfluidics Separation and Analysis of Biological Particles*, Ph.D. thesis (Lund University, 2011).
- ³⁷J. McGrath, M. Jimenez, and H. Bridle, *Lab Chip* **14**, 4139 (2014).
- ³⁸L. Ceriotti, N. F. De Rooij, and E. Verpoorte, *Anal. Chem.* **74**, 639 (2002).
- ³⁹R. Greenwood, P. F. Luckham, and T. Gregory, *J. Colloid Interface Sci.* **191**, 11 (1997).
- ⁴⁰E. S. Asmolov, A. L. Dubov, T. V. Nizkaya, J. Harting, and O. I. Vinogradova, *J. Fluid Mech.* **613**, 613–630 (2017).